AGU PUBLICATIONS

JGR

Journal of Geophysical Research: Atmospheres

RESEARCH ARTICLE
10.1002/2015JD024290

Key Points:
- We developed a global aerosol reconstruction for 1990-2014 using CESM1(WACCM) and volcanic emissions
- Satellite-based forcing data neglect 50-95% of extratropical stratospheric aerosol
- Our output agrees much better with in situ and ground-based observations than standard forcing data

Supporting Information:
- Figure S1 and captions for Tables S1–S4
- Table S1
- Table S2
- Table S3
- Table S4

Correspondence to:
M. J. Mills,
mmills@ucar.edu

Citation:
Mills, M. J., et al. (2016), Global volcanic aerosol properties derived from emissions, 1990–2014, using CESM1(WACCM), *J. Geophys. Res. Atmos., 121*, 2332–2348, doi:10.1002/2015JD024290.

Received 30 SEP 2015
Accepted 12 FEB 2016
Accepted article online 15 FEB 2016
Published online 6 MAR 2016

Global volcanic aerosol properties derived from emissions, 1990–2014, using CESM1(WACCM)

Michael J. Mills[1], Anja Schmidt[2], Richard Easter[3], Susan Solomon[4], Douglas E. Kinnison[1], Steven J. Ghan[3], Ryan R. Neely III[2,5], Daniel R. Marsh[1], Andrew Conley[1], Charles G. Bardeen[1], and Andrew Gettelman[1]

[1]Atmospheric Chemistry Observations and Modeling Laboratory, National Center for Atmospheric Research, Boulder, Colorado, USA, [2]School of Earth and Environment, University of Leeds, Leeds, UK, [3]Atmospheric Sciences and Global Change Division, Pacific Northwest National Laboratory, Richland, Washington, USA, [4]Department of Earth, Atmospheric, and Planetary Sciences, Massachusetts Institute of Technology, Cambridge, Massachusetts, USA, [5]National Centre for Atmospheric Science, University of Leeds, Leeds, UK

Abstract Accurate representation of global stratospheric aerosols from volcanic and nonvolcanic sulfur emissions is key to understanding the cooling effects and ozone losses that may be linked to volcanic activity. Attribution of climate variability to volcanic activity is of particular interest in relation to the post-2000 slowing in the rate of global average temperature increases. We have compiled a database of volcanic SO_2 emissions and plume altitudes for eruptions from 1990 to 2014 and developed a new prognostic capability for simulating stratospheric sulfate aerosols in the Community Earth System Model. We used these combined with other nonvolcanic emissions of sulfur sources to reconstruct global aerosol properties from 1990 to 2014. Our calculations show remarkable agreement with ground-based lidar observations of stratospheric aerosol optical depth (SAOD) and with in situ measurements of stratospheric aerosol surface area density (SAD). These properties are key parameters in calculating the radiative and chemical effects of stratospheric aerosols. Our SAOD calculations represent a clear improvement over available satellite-based analyses, which generally ignore aerosol extinction below 15 km, a region that can contain the vast majority of stratospheric aerosol extinction at middle and high latitudes. Our SAD calculations greatly improve on that provided for the Chemistry-Climate Model Initiative, which misses about 60% of the SAD measured in situ on average during both volcanically active and volcanically quiescent periods.

1. Introduction

Volcanic aerosols and solar variability are the dominant natural drivers of climate variability [*Intergovernmental Panel on Climate Change*, 2013]. Volcanic emissions of sulfur-bearing gases, such as carbonyl sulfide (OCS) and sulfur dioxide (SO_2), produce aerosol particles that scatter solar radiation, reducing solar heating of the surface and atmosphere below them. When the SO_2 from volcanic eruptions is able to reach the stratosphere in significant quantities, such effects can persist for several years and can become hemispheric or global in extent. The rate of stratospheric ozone loss due to anthropogenic halogen emissions is also modulated by heterogeneous chemistry on volcanic aerosols in the stratosphere [*Portmann et al.*, 1996; *Solomon et al.*, 1996].

The effects of small- to moderate magnitude volcanic eruptions since the year 2000 on global climate have been recognized only recently. Previously, it had been assumed that no eruptions since that of Mount Pinatubo in June 1991 had significantly affected stratospheric aerosol optical depths (SAOD) or surface area densities (SADs), the primary parameters affecting climate and chemistry. However, observations have revealed increases in SAOD linked to a series of relatively small-magnitude eruptions since 2005 [*Vernier et al.*, 2011; *Bourassa et al.*, 2012; *Neely et al.*, 2013]. The coincidence of increases in SAOD with a slower rate of increase of globally averaged surface temperatures has led to attributions of their role in contributing to a reduced rate of global warming over the decade of the 2000s [*Solomon et al.*, 2011; *Fyfe et al.*, 2013; *Haywood et al.*, 2013; *Ridley et al.*, 2014; *Santer et al.*, 2014, 2015].

Climate models generally have accounted for stratospheric sulfate aerosols from volcanic eruptions by prescribing aerosol parameters, such as SAOD, mass density ($g\,cm^{-3}$), SAD ($\mu m^2\,cm^{-3}$), and/or effective radius (R_{eff}, μm) and making other assumptions about their size distribution and radiative impact. Such parameters

are generally prescribed based on satellite observations of aerosol extinction, which provide the most continuous near-global record of stratospheric aerosol available. However, analysis of such observations becomes complicated in the lowermost stratosphere by the presence of nearby clouds and variations in tropopause height [*Thomason et al*., 2008; *Thomason and Vernier*, 2013]. Hence, the prescribed stratospheric aerosol parameters used in most climate models are based on satellite analyses that neglect aerosol in the lowermost stratosphere below about 15 km. *Ridley et al*. [2014] used ground-based and in situ observations to show that such satellite analyses therefore neglect a large amount of stratospheric aerosol radiative forcing outside of the tropics, particularly in winter when the extratropical tropopause is well below 15 km.

The primary purpose of this paper is to present the global volcanic aerosol properties calculated using a new prognostic stratospheric aerosol capability in Community Earth System Model (CESM) and a new volcanic SO_2 emissions database for the years 1990–2014. We compare model output to observations and to the volcanic aerosol distributions prescribed for the Chemistry-Climate Model Initiative (CCMI) [*Eyring et al*., 2013], which have been or are being used in many current and recent model studies. We first describe updates to CESM used in our simulations, including the new prognostic stratospheric aerosol capability and volcanic SO_2 emissions. Our global aerosol properties are available for download from the Earth System Grid and may be used for forcing climate and chemistry in models lacking prognostic stratospheric aerosols.

2. Model Description

2.1. CESM1(WACCM)

The Community Earth System Model, version 1 (CESM1) [*Hurrell et al*., 2013], is a state-of-the-art global climate model that includes interactive atmosphere, ocean, land, and sea-ice components. The atmosphere component of CESM is the Community Atmosphere Model (CAM), which includes a high-top version known as the Whole Atmosphere Community Climate Model (WACCM) [*Marsh et al*., 2013]. Low-top CAM extends from the surface to the middle stratosphere (~40 km) and may be run with prescribed ozone (hereafter CAM) or with detailed interactive chemistry (CAM-chem) [*Lamarque et al*., 2012]. We have developed a new prognostic capability for calculating stratospheric aerosol properties from source-gas emissions, for use in CESM with CAM, CAM-chem, or WACCM. Here we describe its implementation in WACCM, which includes the most complete treatment of the stratosphere.

WACCM extends up to 140 km in altitude and integrates atmospheric chemistry and physics from the troposphere up to the lower thermosphere. Here we use WACCM with the more realistic formulations of radiation, planetary boundary layer turbulence, cloud microphysics, and aerosols that were introduced in version 5 of CAM [*Neale et al*., 2010]. In particular, aerosols are represented in a prognostic modal aerosol model (MAM) [*Liu et al*., 2012], and direct effects of aerosols are included in the radiation code. Indirect effects of sulfur and black and organic carbon are included in the cloud microphysics [*Morrison and Gettelman*, 2008; *Gettelman et al*., 2010]. As described below, we have adapted the CAM5 physics for WACCM, updated the chemistry to include species important in the troposphere as well as the middle atmosphere, and modified MAM to simulate the evolution of stratospheric sulfate aerosol from volcanic and nonvolcanic emissions. Our extension of CAM5 physics improvements to WACCM required several adaptations and bug fixes for the higher model top. The merging of mesospheric with lower-atmospheric heating rates just above the stratopause has been revised from CESM1(WACCM) with CAM4 physics [*Marsh et al*., 2013] and is described in Appendix A.

We merge previous chemistry modules appropriate for the troposphere, stratosphere, mesosphere, and lower thermosphere into a unified "TSMLT" mechanism for WACCM. The middle atmosphere chemistry described in *Marsh et al*. [2013] has been extended to include nonmethane hydrocarbons important for tropospheric photochemistry [*Lamarque et al*., 2012]. The TSMLT chemical scheme includes 158 photochemical species (supporting information Table S1 and Table A3); 2 invariant species; 117 photolysis reactions (Table S2); 331 gas-phase reactions (Table S3); 2 aqueous-phase reactions in cloud droplets (Table A1); 4 heterogeneous reactions on tropospheric aerosols (Table A1); and 6 heterogeneous reactions on stratospheric aerosols, with varying rates for sulfate, nitric acid trihydrate, and water ice (Table A2). Sulfur-bearing gases include dimethyl sulfide (DMS) and SO_2 as in *Lamarque et al*. [2012], to which we add OCS, SO, S, SO_3, and H_2SO_4. OCS is largely inert in the troposphere but is oxidized and photolyzed in the stratosphere to produce much of the sulfate present in nonvolcanic periods [*Junge et al*., 1961; *Chin and Davis*, 1995; *Brühl et al*., 2012; *Sheng et al*., 2015b]. We use a new time-varying lower boundary condition for OCS based on the ice core, firn air, and ambient air data presented in *Montzka et al*. [2004] from 1765

to 2010. After 2010, the OCS lower boundary condition is held at an approximately present-day volume mixing ratio of 5.10×10^{-10} molecules OCS/molecule air. Anthropogenic emissions of SO_2 and DMS are included, as described in *Lamarque et al*. [2012]. We include H_2SO_4 photolysis by visible light, based on the empirical work of *Feierabend et al*. [2006], which increases rates compared to previous theoretical studies [*Hintze et al*., 2003; *Vaida et al*., 2003]. H_2SO_4 photolysis cross sections for visible light incorporate pressure-dependent quantum yields to include the effects of band-dependent quenching of vibrationally excited states [*Miller et al*., 2007]. We also include H_2SO_4 photolysis by Lyman α [*Lane and Kjaergaard*, 2008].

We include the CAM5 modal treatment of tropospheric aerosol, including sulfate, which is coupled to cloud microphysics. Our study employs the three-mode version of the Modal Aerosol Model (MAM3) [*Liu et al*., 2012], which represents the aerosol as three lognormal modes (Aitken, accumulation, and coarse) composed of internal mixtures of soluble and insoluble components (Table A3). The total number mixing ratio and the mass mixing ratio of each component are predicted for each mode, while the mode width is prescribed. MAM3 is capable of representing aerosol microphysical processes, such as nucleation, condensation, coagulation, and sedimentation. MAM3 calculates new particle formation using the parameterization of binary H_2SO_4-H_2O homogeneous nucleation of *Vehkamaki et al*. [2002]. Aerosol optical, physical, and chemical properties are treated in a physically based manner. We have adapted and extended MAM3 to include a new prognostic stratospheric aerosol option, as described in Appendix B.

Heterogeneous chemistry is fully connected to aerosol properties from MAM3. Reactions between the gas and aerosol phases are parameterized based on MAM3 aerosol SAD. As was done in CAM5-chem for the tropospheric heterogeneous reactions described by *Tilmes et al*. [2015], stratospheric heterogeneous reactions use SAD derived from the mass and hydrated size distributions of sulfate, black carbon, and organic aerosols. Sea salt and mineral dust aerosols do not contribute to the SAD used for chemistry, as heterogeneous reactions are assumed to not occur on these surfaces. We calculate hydrated SAD for each mode using the known relation between the surface area and the three parameters of a lognormal distribution [*Seinfeld and Pandis*, 1998] and sum the three modes for use in heterogeneous chemistry.

WACCM may be run in a free-running (FR) mode or nudged with specified dynamics (SD). FR-WACCM runs self-consistent interactive atmospheric chemistry, radiation, and dynamics. We have added four vertical layers in the boundary layer to match CAM5, for a total of 70 vertical levels from the surface to 5.1×10^{-6} hPa. SD-WACCM calculates the same chemistry and physics as FR-WACCM before meteorological fields and temperatures are adjusted [*Lamarque et al*., 2012; *Wegner et al*., 2013]. SD-WACCM improves representation of atmospheric dynamics and temperatures for the study of specific years of observations, compared to FR-WACCM. Our SD-WACCM runs use meteorological fields from the NASA Global Modeling and Assimilation Office Modern-Era Retrospective Analysis for Research and Applications (MERRA) [*Rienecker et al*., 2011] and run with 88 vertical levels to match MERRA. Temperature, zonal and meridional winds, and surface pressure are used to drive the physical parameterizations that control boundary layer exchanges, advective and convective transport, and the hydrological cycle. In the present study, the WACCM meteorological fields are relaxed with a 50 h relaxation time toward the MERRA reanalysis fields implemented between the surface and 50 km, using the approach described in *Kunz et al*. [2011]. The nudging is reduced linearly between 50 and 60 km, with zero nudging above 60 km. We run WACCM on a 1.9° latitude × 2.5° longitude horizontal grid, as in *Marsh et al*. [2013]

2.2. Volcanic Eruption Database

We have compiled a database of climatically relevant volcanic SO_2 emissions and plume altitudes for eruptions from 1990 to 2014 (supporting information Table S4). Climatically relevant emissions are those that remain in the atmosphere after a few days and are not scavenged by ash. The eruptions in Table S4 have been detected by one or more satellite instruments including Total Ozone Mapping Spectrometer (TOMS), Ozone Monitoring Instrument, Ozone Mapping and Profiler Suite, Infrared Atmospheric Sounding Interferometer, Global Ozone Monitoring Experiment, Atmospheric Infrared Sounder, Microwave Limb Sounder (MLS), or the Michelson Interferometer for Passive Atmospheric Sounding instrument. We predominately used published estimates of the eruption source parameters and reports from the Smithsonian Global Volcanism Program (http://volcano.si.edu/), NASA's Global Sulfur Dioxide Monitoring website (http://so2.gsfc.nasa.gov/) as well as the Support to Aviation Control Service (http://sacs.aeronomie.be/). We do not restrict the inclusion of an eruption based on its volcanic explosivity index (VEI) [*Newhall and Self*, 1982] or the emission height of the SO_2 (i.e., our database

includes volcanic eruptions that emitted SO_2 into the troposphere only, as well as direct stratospheric emissions). For the model simulations, volcanic SO_2 is emitted over a 6 h period between 12:00 UTC and 18:00 UTC on each day of eruption at the nearest model column. Volcanic SO_2 emissions are distributed vertically between the minimum and maximum altitudes of the eruption plume at a constant emission rate per unit volume, based on the best estimates for SO_2 mass and vertical plume distribution available (supporting information Table S4). Emissions from continuously degassing volcanoes are also included using the emission inventory of *Andres and Kasgnoc* [1998]. Note that the version of the database used for the model simulations does not include SO_2 emissions from the long-lasting effusive fissure eruptions of Tolbachik (active from November 2012 to August 2013), Bárdarbunga/Holuhraun (active from 29 August 2014 to 27 February 2015), and Fogo (23 November 2014 to 8 February 2015). These eruptions likely had negligible impact on the stratosphere, as they emitted into the lowermost troposphere.

For the model simulations of the 1991 Mount Pinatubo eruption, we emit 10 Tg of SO_2 into grid cells between the equator and 15°N at the longitude of eruption (120°E), accounting for the initial spread southward of the volcanic cloud based on TOMS observations of the SO_2 cloud on 16–18 June 1991 [*Bluth et al*., 1992]. Our analysis of the initial spread of SO_2 from numerous eruptions suggests that a single-column emission is suitable for eruptions with VEI 4 or less, while larger initial areas may be suitable for VEI 5 and 6 eruptions. Our eruption database includes only three eruptions with VEI larger than four (Pinatubo 1991, VEI 6; and Cerro Hudson 1991 and Puyehue-Cordón Caulle 2011, VEI 5). Our model does not currently simulate volcanic ash or water vapor emissions nor consequent ice sequestration of SO_2 and fallout of ash and ice particles, which took place mainly during the first 4–5 days of the 1991 Pinatubo eruption [*Guo et al*., 2004]. In the model, we therefore reduce the mass of SO_2 emitted to 10 Tg of SO_2, which corresponds to the mass detected by TIROS Operational Vertical Sounder and TOMS 7–9 days after the beginning of the eruption, when more than 99% of the ash and ice particles were removed [*Guo et al*., 2004]. This is what we consider to be the "climatically relevant" portion of the 1991 Mount Pinatubo SO_2 emissions for our model. The neutral buoyancy height of the volcanic plume produced by the 15–16 June 1991 Pinatubo climatic phase was about 24 km [*Koyaguchi and Tokuno*, 1993] and the maximum overshooting height was 40 km [*Holasek et al*., 1996]. For both the free-running and the specified dynamics simulations, we find best agreement with MLS observations of the SO_2 cloud on 21 September 1991 [*Read et al*., 1993] when emitting SO_2 uniformly into model grid boxes between 18 km and 20 km, allowing for lofting of SO_2 (and sulfuric acid aerosol particles) over time (see Figure S1).

Several other recent modeling studies also find best agreement with the Stratospheric Aerosol and Gas Experiment (SAGE) II observations when emitting between 10 Tg and 14 Tg of SO_2 [*Dhomse et al*., 2014; *Sheng et al*., 2015a], which suggests that models that neglect in-plume processes such as scavenging of SO_2 on volcanic ash and ice particles ought to be initialized using a lower total SO_2 mass (the "climatically relevant mass") than initially emitted by the 15 June 1991 eruption of Mount Pinatubo. *Brühl et al*. [2015] simulated Pinatubo with 17 Tg of SO_2 and calculated peak tropical average SAOD values that were 50% higher than were observed by SAGE, although this could be explained by saturation issues in the SAGE observations in the tropics during the peak after Pinatubo. We have performed a simulation using 12 Tg of SO_2 for Pinatubo and found that it produces somewhat higher optical depths than observed by lidars at Geesthacht, Germany in 1991–1993 [*Ansmann et al*., 1997] and at Mauna Loa in 1994–1995 [*Hofmann et al*., 2009].

3. Model Simulations

We performed three simulations of the period 1 January 1990 to 30 November 2014 using SD-WACCM. Our NOVOLC simulation ran for the entire period without the new volcanic SO_2 emissions database but with emissions from continuously degassing volcanoes and from anthropogenic emissions, as well as from DMS and OCS oxidation. Our VOLC simulation adds the volcanic SO_2 emissions in database (Table S4). It includes all natural and anthropogenic SO_2 emissions. Our PIN12 simulation uses 12 Tg SO_2 for Pinatubo, rather than 10 Tg, but otherwise includes identical emissions to the VOLC simulation. See Appendix C for details on the model initialization.

Additionally, we used FR-WACCM to examine the heating of the stratosphere due to stratospheric aerosol following the 1991 Pinatubo eruption. We ran an ensemble of four FR simulations covering the period 1990–1993. Each used the same 10 Tg SO_2 emission for Pinatubo input at 18–20 km, as well as the other eruptions from our database.

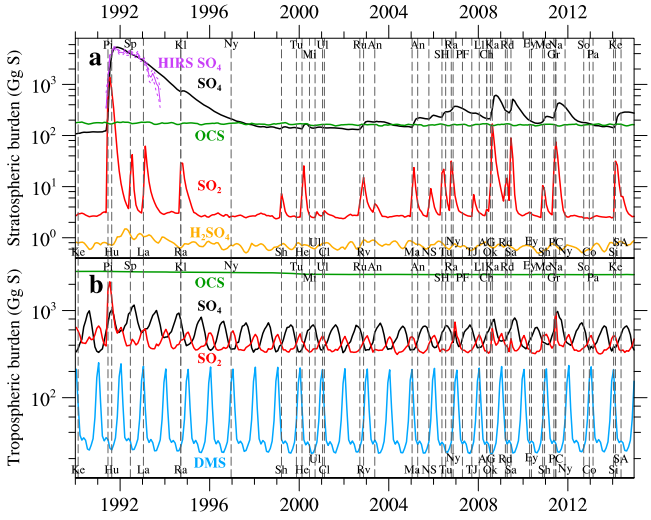

Figure 1. The calculated global mass burdens of major sulfur-bearing species from our SD-WACCM VOLC simulation (a) above the tropopause and (b) below the tropopause are shown as a function of time from 1 January 1990 to 31 July 2014. Mass burdens are shown in units of Gg (=10^9 g) of S. The burdens of DMS in the stratosphere (10^{-3}–10^{-2} Gg S) and of H_2SO_4 in the troposphere (1–4 Gg S) are too small to be shown. Sulfate aerosol mass is also shown from High Resolution Infrared Radiation Sounder (HIRS) observations, 80°S–80°N, scaled from total aerosol mass (assuming 75% H_2SO_4 by mass) presented in *Baran and Foot* [1994]. *Baran and Foot* [1994] estimate an uncertainty in the HIRS observations of 1.4 Tg aerosol (0.34 Tg S), shown as dashed purple lines. Initial dates of eruptions included in the volcanic SO_2 database (Table S4) used in the simulation are shown as vertical dashed lines, with two-character identifiers of the eruptions as follows: AG = Cerro Azul Galapagos, An = Anatahan, Ch = Chaiten, Cl = Cleveland, Co = Copahue, Ey = Eyjafjallajoekull, Gr = Grimsvoetn, He = Hekla, Hu = Cerro Hudson, Ka = Kasatochi, Ke = Kelut, Kl = Kliuchevskoi, La = Lascar, Ll = Llaima, Ma = Manam, Me = Merapi, Mi = Miyake jima, Na = Nabro, NS = Negra Sierra, Ny = Nyamuragira, Ok = Okmok, Pa = Paluweh, PC = Puyehue Cordon Caulle, PF = Piton de la Fournaise, Pi = Pinatubo, Ra = Rabaul, Rd = Redoubt, Ru = Ruang, Rv = Reventador, Sa = Sarychev Peak, SA = Sangeang Api, Sh = Shishaldin, SH = Soufriere Hills, Sh = Sheveluch, Si = Sinabung, So = Soputan, Sp = Spurr, TJ = Tair Jebel at, Tu = Tungurahua, and Ul = Ulawun.

The FR runs were initialized with small roundoff level differences in their atmospheric states, producing unique trajectories from internally generated climate variability alone. Our FR and SD simulations were run with specified historical sea surface temperatures (SSTs) based on observations from the period simulated [*Hurrell*, 2008].

4. Results and Discussion

4.1. Sulfur Chemical Budget

Figure 1 shows the global burdens of the dominant sulfur-bearing gases and aerosols in the stratosphere and in the troposphere from our VOLC simulation. The initial dates of volcanic eruptions included in our database are indicated by vertical dashed lines, with two-letter identification codes consistent with Table S4. The burdens of DMS in the stratosphere (10^{-3}–10^{-2} Gg S) and of H_2SO_4 in the troposphere (1–4 Gg S) are too small to be shown. In the troposphere, short-lived DMS, SO_2, and sulfate aerosol exhibit strong seasonal cycles based on seasonal emissions, with some volcanic perturbations. Long-lived OCS displays a constant global burden in the troposphere and in the stratosphere. OCS dominates the S budget in both regions in most periods. We calculate an OCS mass burden that is comparable below the tropopause but 35–45% lower above the tropopause than that calculated by *Sheng et al.* [2015b]. During the volcanically quiescent period of 2000–2001, our stratospheric sulfate burden is 138 Gg S, compared to 115 Gg S derived using the SAGE_4λ method [*Arfeuille et al.*, 2013, 2014].

Large enhancements in stratospheric SO_2 are evident in the months immediately following volcanic eruptions with large SO_2 inputs to the stratosphere. The 1991 eruption of Mount Pinatubo is believed to have had the greatest global impact on stratospheric aerosol since Krakatau erupted in 1883 [*Self et al.*, 1993]. In the stratosphere, oxidation, nucleation, and condensation pathways produce sulfate aerosol from SO_2 with an *e*-folding time of about 1 month. Volcanically enhanced sulfate aerosols persist in the stratosphere until sedimentation and troposphere-stratosphere exchange remove them, with an *e*-folding time of about 0.8–1.5 years [*Deshler*, 2008], depending on its latitude and height of penetration into the stratosphere. In WACCM, global stratospheric sulfate mass burden peaks at ~5.3 Tg S in late 1991, following our 10 Tg SO_2 injection mass from Pinatubo (the molecular mass of SO_2 being almost exactly double the atomic mass of S). This compares well to the total sulfate burden derived from High Resolution Infrared Radiation Sounder (HIRS) observations, 80°S–80°N, also shown in Figure 1, adapted from total aerosol burdens presented by *Baran and Foot* [1994]. The HIRS observations peak at ~5.6 Tg S and confirm our calculated burdens in the

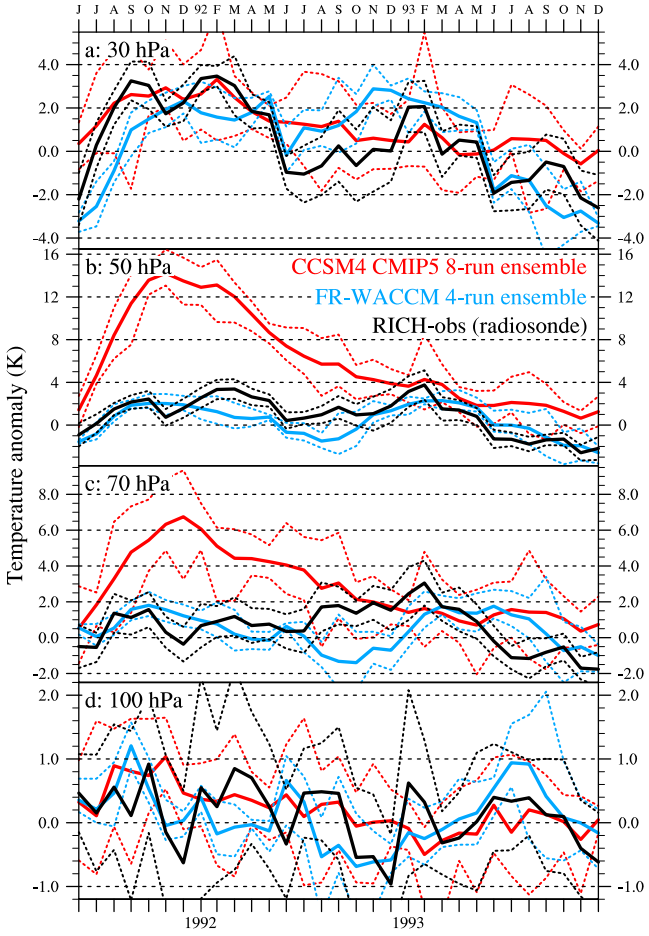

Figure 2. Post-Pinatubo monthly average stratospheric tropical (20°S–20°N) temperature anomalies are shown with respect to corresponding monthly mean values for June 1990–May 1991. Global radiosonde temperature observations compiled with the Radiosonde Innovation Composite Homogenization (RICH-obs) software package [*Haimberger et al.*, 2012] are shown in black. Solid black lines show the average, and dashed black lines show the standard deviation, of the gridded observations. Corresponding tropical anomalies from an ensemble of four FR-WACCM simulations with historical SSTs are shown in blue. Tropical temperatures from an ensemble of eight CMIP5 runs using CCSM4 with prescribed volcanic aerosols are shown in red. Solid lines show ensemble averages; dashed lines show ensemble maxima and minima monthly average anomalies.

18 months following the 1991 Pinatubo eruption. *Baran and Foot* [1994] estimate an uncertainty of 0.34 Tg S, which is ~2.5 times higher than our calculated stratospheric background aerosol load.

4.2. Stratospheric Volcanic Aerosol Heating

Significant increases in temperature in the tropical lower stratosphere were observed following the volcanic eruptions of Agung (March 1963), El Chichón (April 1982), and Mount Pinatubo (June 1991) [*Randel*, 2010]. RICH-obs v1.5.1 is the latest version of global radiosonde temperature observations from 1958 to present homogenized with the Radiosonde Innovation Composite Homogenization (RICH) software package [*Haimberger et al.*, 2008, 2012]. Figure 2 shows monthly mean (solid black lines) and standard deviation (dashed black lines) of the RICH-obs temperature anomalies in the tropical (20°S–20°N) lower stratosphere for the post-Pinatubo period, June 1991 to December 1993. All temperature anomalies shown in Figure 2 were normalized and deseasonalized by subtracting corresponding monthly mean values from June 1990 to May 1991. The purpose of this is to present a consistent comparison between observations and model calculations, rather than identifying a volcanic signal in the temperatures. The latter would require removing the effects of ocean states, such as the El Niño–Southern Oscillation, from the observations. Corresponding tropical temperature anomalies from our FR-WACCM four-member ensemble, which incorporate ocean state influences with historical SSTs, are shown in blue. The thick solid blue line shows the ensemble average for each month, and the thinner dashed blue lines show the maximum and minimum of monthly-averaged temperatures across the four ensemble members. Tropical temperature anomalies from an ensemble of eight CCSM4 runs for the Coupled Model Intercomparison Project Phase 5 (CMIP5) are shown in red [*Meehl et al.*, 2012]. CCSM4 includes CAM4 with prescribed volcanic aerosols, fully coupled to an ocean.

In general, WACCM does an excellent job of reproducing the temperature increases observed in the lower stratosphere. The largest temperature increases in the 12 months following the eruption are 3–4 K at the 30 and 50 hPa levels. WACCM matches these well. At 70 and 100 hPa, the WACCM ensemble reproduces well the magnitude and variability within the observed warming, with significant departures only during August, October, November, and December of 1992, when calculated temperature anomalies were colder than those

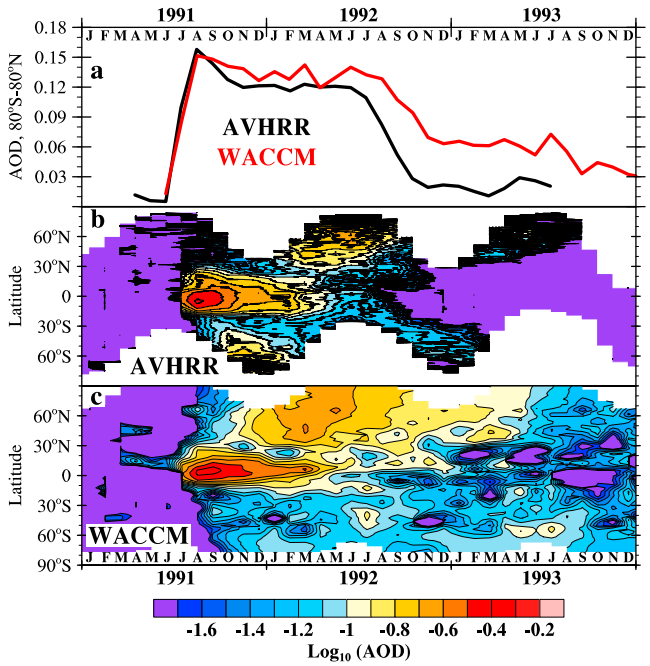

Figure 3. (a) Monthly global average total AOD over oceans measured at 0.63 μm by AVHRR (black curve) and calculated at 0.55 μm from our SD-WACCM VOLC simulation (red curve), following the June 1991 Pinatubo eruption. Model averages are masked to remove latitudes not present in AVHRR observations for each month. Average AOD values for the year 1990 are subtracted from observations and calculations. (b) Monthly zonal average AVHRR AOD over oceans minus background values taken from 1990 zonal mean values for corresponding months. (c) Monthly zonal average SD-WACCM VOLC AOD calculations over oceans minus background values taken from 1990 zonal mean values for corresponding months. A logarithmic scale is shown for Figures 3b and 3c.

observed. In contrast, CCSM4 vastly overheats the lower stratosphere after Pinatubo, with temperature increases of 12–16 K at 50 hPa and 4–9 K at 70 hPa. This is largely due to an excess of sulfate mass in the prescribed volcanic forcing file used in CCSM4, which peaked at 8.8 Tg S in October 1991. Such a sulfate burden would require more than 17 Tg SO_2 from the 1991 Pinatubo eruption.

4.3. Stratospheric Aerosol Optical Depths

Figure 3 compares SD-WACCM calculations following the 1991 Pinatubo eruption to aerosol optical depth (AOD) measurements from the Advanced Very High Resolution Radiometer (AVHRR) satellite instrument, which makes observations over global oceans [*Zhao et al.*, 2013]. Figure 3a compares the monthly mean AOD over global oceans from AVHRR to SD-WACCM. We removed latitudes not observed by AVHRR for each month from our SD-WACCM average. We removed background values from both curves, calculated as 1990 annual average values from observations and calculations. Figures 3b and 3c show zonal mean AOD over oceans from AVHRR and SD-WACCM, respectively. We removed background values, calculated as zonal mean values for corresponding months in 1990. AVHRR confirms the timing and magnitude of our calculated peak monthly global AOD value of 0.15 in August 1991 and matches our calculated evolution for 12 months following the eruption. In the second half of 1992, AVHRR global AOD drops off faster than our calculations. As shown in Figure 3b, this is related to a lack of AOD at low latitudes in AVHRR observations. The model matches well the observed zonal evolution of Pinatubo AOD for the first 12 months after the eruption.

Figure 4a shows zonal monthly mean SAOD in the visible (integrated 550 nm-centered extinction above the model-diagnosed local World Meteorological Organization (WMO) lapse rate tropopause level) from January 1991 to November 2014 from our VOLC simulation. Volcanic eruptions included in our database are labeled at the latitude and time of initial eruption. SAOD is elevated in the period from June 1991 to mid-1997, mostly from the 1991 Pinatubo eruption. SAOD reaches a relatively flat minimum over the period 1998 to 2003, before rising again due to a number of small and moderate eruptions that put SO_2 in the upper troposphere and stratosphere.

Figure 4b shows AOD levels for the entire atmosphere (integrated extinction from the surface to the top of the model) for VOLC minus NOVOLC simulations. Subtracting the NOVOLC simulation reveals the perturbations due to our volcanic SO_2 database, including numerous small eruptions that added sulfate to either the troposphere or stratosphere that are not evident in the total SAOD panel. Figure 4b also reveals when and where aerosol levels reach their nonvolcanic background, such as from 1998 to 2003. Even during this period, however, aerosols from the emissions of several small eruptions are evident at specific latitudes and times, in particular at high northern latitudes. This illustrates the difficulty of assessing a true nonvolcanic "background" SAOD level from observations alone.

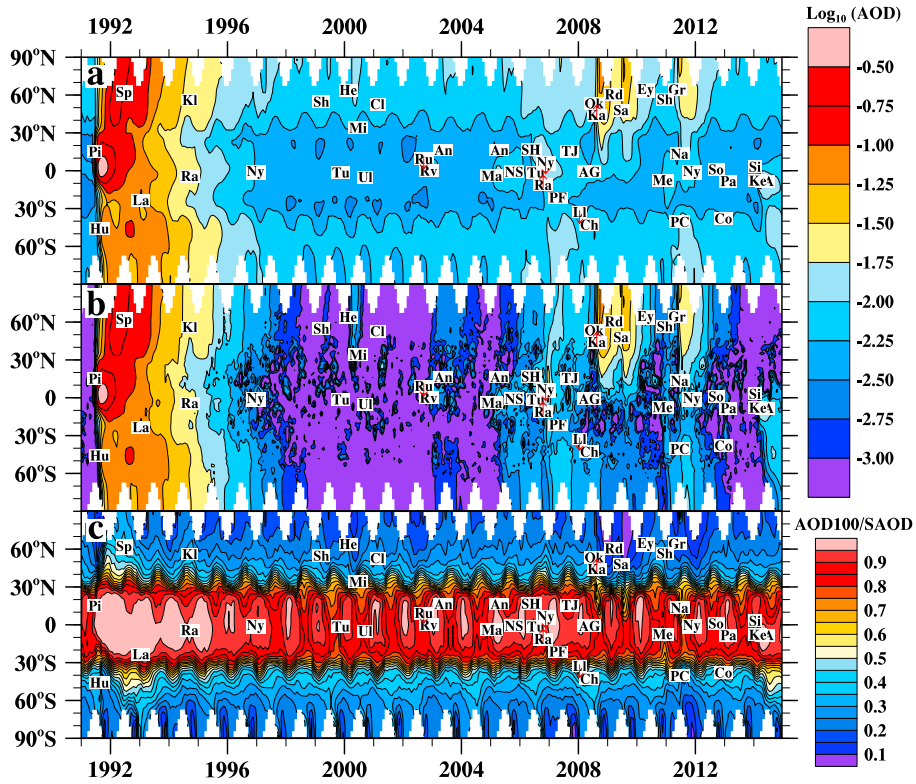

Figure 4. (a) Zonal monthly mean SAOD (integrated extinction above the model's diagnosed tropopause) in the visible are shown from January 1991 to July 2014 from our SD-WACCM VOLC simulation. (b) AOD levels for the entire atmosphere (integrated extinction from the surface to the top of the model) are shown for VOLC minus NOVOLC simulations. A logarithmic scale is shown for Figures 4a and 4b. (c) The ratio of AOD100 (aerosol optical depth integrated for pressures less than 100 hPa) to SAOD is shown. AOD100 corresponds to the AOD retrieved from available satellite observations, which typically integrate aerosol extinction only above 15 km to reduce potential contamination by clouds. The ratio therefore shows the fraction of SAOD typically captured in satellite-based climatologies. Volcanic eruptions are labeled at the latitude and time of the initial eruption, using the codes from Figure 1 and Table S4.

Satellite observations typically integrate aerosol extinction only above 15 km to reduce potential contamination by clouds. We define AOD100 as aerosol optical depth integrated for pressures less than 100 hPa, to correspond to satellite observations. Figure 4c shows the fraction in our VOLC simulation of SAOD that is contributed by AOD100. Our calculations confirm the analysis of *Ridley et al*. [2014], which was based on comparison of ground-based and satellite observations, that aerosol loading between the tropopause and 15 km (~100 hPa) contributes at least 30 to 70% of the total SAOD, and that this percentage can increase further following eruptions. Poleward of about 40° latitude in both hemispheres, the AOD100 is always less than 50% of SAOD and diminishes rapidly with latitude to ~25% at 60°N, and ~20% at 70°N. Immediately following eruptions such as Kasatochi (2008) and Sarychev (2009), we calculate more than 10 or 15 times as much AOD above the tropopause as above 100 hPa at high northern latitudes.

Figure 5 shows our VOLC simulation zonal mean SAOD (black solid curves) and AOD100 (black dashed curves) at four different latitudes, compared to local lidar observations, and satellite analyses. *Ansmann et al.* [1997] and *Ridley et al*. [2014] provide extinction derived from lidar 532 nm backscatter measurements, using techniques such as those described in *Jäger and Deshler* [2002]. *Ridley et al*. [2014] used University of Wyoming balloon-borne optical particle counter (OPC) measurements to confirm that a lidar extinction to backscatter ratio of 50 is still appropriate to the stratosphere and accurate to an uncertainty of 10–20%. Figure 5a shows a latitude-weighted 60–90°N average of model calculations. In the period from 1998 to 2004, there was little if any perturbation from volcanic eruptions, and our calculated SAOD is ~0.01, and AOD100 is ~0.002, indicating that ~80% of the SAOD is below 15 km. The available lidar measurements above 10 km at Ny-Ålesund (78.9°N, 11.9°W) from January to September 2008 and February to September 2009 [*Ridley et al*., 2014; *Hoffmann*, 2011] show excellent agreement

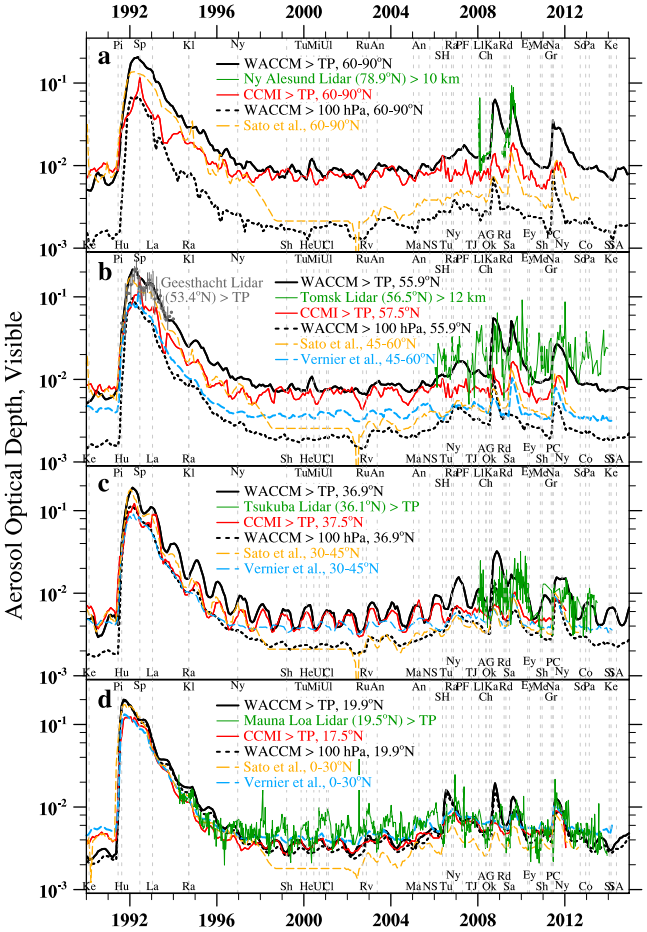

Figure 5. SD-WACCM VOLC simulation zonal mean calculations for SAOD (black solid curves) and AOD100 (black dashed curves) at four different latitudes are compared to lidar observations (green curves and grey circles), the CCMI extinction climatology integrated above the WACCM calculated tropopause (red solid curves), and the climatologies of Sato et al. (orange dashed curves) and Vernier et al. (blue dashed curves). The temporal resolution of lidar measurements presented is generally daily to weekly outside of data gaps. Minor ticks on the vertical axis indicate values 2, 4, 6, and 8 times the major tick below. (a) Lidar measurements above 10 km at Ny-Ålesund (green curves, 78.9°N, 11.9°W) from January to September 2008 and February to September 2009 [*Ridley et al.*, 2014; *Hoffmann*, 2011] are compared to latitude-weighted 60–90°N averages of WACCM calculations and climatologies. (b) Lidar measurements above the tropopause at Geesthacht (grey circles with 1σ error bars, 53.4°N, 10.4°E) from August 1991 to December 1992 [*Ansmann et al.*, 1997], and above 12 km at Tomsk (green curves, 56.5°N, 85.0°E) from January 2006 to December 2013 [*Bazhenov et al.*, 2012], are compared to WACCM at 55.9°N, CCMI at 57.5°N, and Sato et al. and Vernier et al. at 45-60°N. (c) Lidar measurements above the tropopause at Tsukuba (green curves, 36.1°N, 140.1°E) from January 2008 to July 2013 [*Uchino et al.*, 2012] are compared to WACCM at 36.9°N, CCMI at 37.5°N, and Sato et al. and Vernier et al. at 30–45°N. (d) Lidar measurements above the tropopause at Mauna Loa (green curves, 19.5°N, 155.6°W) from April 1994 to December 2013 [*Hofmann et al.*, 2009] are compared to WACCM at 19.9°N, CCMI at 17.5°N, and Sato et al. and Vernier et al. at 0–30°N. Initial dates of the eruptions are shown as in Figure 1.

with our calculations, including the sharp rises in AOD following the eruptions of Kasatochi (8 August 2008) and Sarychev (15 June 2009). In contrast, the satellite analysis of *Sato et al.* [1993], updated on the NASA Goddard Institute for Space Studies website, and hereafter referred to as Sato et al., derives an SAOD at 60–90°N (orange curve) that is smaller by a factor of 5 to 10 in 2008–2009 than our calculations and the lidar measurements. In fact, for all times after 1997, the SAODs of Sato et al. in this latitude band are much closer to WACCM's calculated AOD100 than to WACCM's total SAOD. Stratospheric aerosol extinction values are provided for use in CCMI simulations based on the SAGE_4λ method [*Arfeuille et al.*, 2013, 2014]. We have integrated these above the tropopause height derived in our SD-WACCM runs to show CCMI SAOD values (red curve). While the CCMI SAOD values at 60–90°N compare well to WACCM during the low volcanic period from 1998 to 2004, they fall below our calculations during the 1991 Pinatubo and post-2004 volcanic periods. The satellite-derived volcanic forcing used for CCMI misses much of the volcanic aerosol in the lowermost stratosphere at Northern high latitudes.

Figure 5b compares WACCM SAOD calculations at 55.9°N to lidar measurements above the tropopause at Geesthacht (53.4°N, 10.4°E) from August 1991 to December 1992 [*Ansmann et al.*, 1997] and above 12 km at Tomsk (56.5°N, 85.0°E) from January 2006 to December 2013 [*Bazhenov et al.*, 2012]. The comparison to the Geesthacht measurements is excellent for the 10 Tg SO_2 Pinatubo simulation. Our PIN12 simulation (not shown) produced SAOD values that were slightly higher than those observed in 1992 and that were in the upper end of the range of measurement uncertainties in 1991 and 1993. Comparison of our calculated SAOD to the Tomsk measurements are also quite good, and show particularly excellent agreement following the 2008 Kasatochi and 2009 Sarychev eruptions. In addition to the Sato et al. analysis for 45–60°N (orange curve), we add an updated version of the merged SAOD data

developed by *Vernier et al.*, [2011], (blue curve, hereafter referred to as Vernier et al.). Again we note that, after 1997, Sato et al. closely matches our AOD100, rather than SAOD. During the low volcanic period of 1997–2004, Vernier et al. is higher than Sato et al. but is still only about 40% of our calculated SAOD. During the 1991–1996 post-Pinatubo period, Vernier et al. is lower than Sato et al. and very closely matches our AOD100. After 2004, Vernier et al. and Sato et al. very closely match each other and are a factor of 5–10 lower than the Tomsk lidar and our calculated SAOD. The CCMI SAOD values at 57.5°N (red line) again match our calculations only during the volcanically quiescent period of 1997–2004 and are a factor of 2–4 lower than our calculated SAOD after 2005.

Figure 5c compares WACCM SAOD calculations at 36.9°N to lidar measurements above the tropopause at Tsukuba (36.1°N, 140.1°E) from January 2008 to July 2013 [*Uchino et al*., 2012]. Here we find good agreement between our calculations and the measurements, apart from a prominent calculated peak following the 2008 Kasatochi eruption that is not evident in the observations. Apart from the 12 months following Kasatochi, our calculated SAODs match the observations somewhat better than Sato et al., Vernier et al., or CCMI. During the low volcanic period of 1997–2004, Vernier et al. and CCMI match our calculations well, while Sato et al. are low by at least a factor of 2 and match our calculated AOD100. The annual oscillation most evident during this low volcanic period in SAOD from WACCM and CCMI is related to the stronger transport of aerosol from the tropics to the winter hemisphere than to the summer hemisphere with the lower branch of the Brewer-Dobson circulation [e.g., *Holton et al*., 1995], as well as to the minimum in tropopause height in the winter.

Figure 5d compares WACCM SAOD calculations at 19.9°N to lidar measurements above the tropopause at Mauna Loa (19.5°N, 155.6°W) from April 1994 to December 2013 [*Hofmann et al*., 2009]. Our SAOD in 1994–1995 is slightly higher than was observed at Mauna Loa. Calculated SAOD in this period were higher still in our PIN12 simulation (not shown). In general, however, our calculated SAOD matches the lidar measurements about as well as the satellite-derived climatologies throughout the comparison period. The observations exhibit a larger seasonal cycle than we calculate, and at their seasonal peak are about twice our calculations during the relatively quiescent period of 1998–2004. This may trace to meteoritic impacts on the assumed lidar Rayleigh background as described in *Neely et al*. [2011]. It may also be due to a seasonal change in the latitudinal history of air masses observed over Mauna Loa, which is at the boundary between the tropics and midlatitudes. This is a subtlety that our model might miss due to its resolution. An improved atmospheric extinction model has been applied to the post-2002 Mauna Loa lidar measurements, reducing the apparent seasonal cycle (John Barnes, personal communication). We calculate higher SAOD following the Soufriere Hills (2006), Kasatochi (2008), and Sarychev (2009) eruptions than were observed at Mauna Loa. Our SAOD following the Nabro eruption (2011) matches well that observed at Mauna Loa and Tomsk. The Vernier et al. and CCMI SAOD values compare much better to Mauna Loa measurements than to lidars at higher latitudes, as the tropical tropopause is close to the 15 km lower limit of satellite analyses. Sato et al. are notably lower than the Mauna Loa lidar observations and our calculations.

The differences in SAOD that we calculate are significant enough to affect global average surface temperatures. *Ridley et al*. [2014] calculate that SAOD consistent with ground-based lidar and radiometer observations would produce a median reduction in global average temperature of about 0.08°C in 2012, roughly double the cooling calculated using Vernier et al. and Sato et al. Use of our calculated aerosol properties should enhance the ability of climate models without prognostic stratospheric aerosols to reproduce and understand historical changes in surface temperature.

4.4. Stratospheric Aerosol Surface Area Densities

SAD is an important parameter in calculating heterogeneous chemical reactions in the stratosphere that affect ozone and related species [*Hofmann and Solomon*, 1989; *Rodriguez et al*., 1991; *Fahey et al*., 1993; *Mills et al*., 1993; *Solomon et al*., 1996, 2015]. Global models that include stratospheric chemistry therefore rely on SAD derived from satellite observations, which provide the best global coverage [e.g., *Stratospheric Processes and their Role in Climate*, 2010; *Arfeuille et al*., 2014]. Here we compare SAD calculated from our simulations to SAD provided for the CCMI experiments, as well as to SAD derived from in situ measurements of aerosol size.

The University of Wyoming balloon-borne OPC has provided a consistent record of in situ vertical profiles of size-resolved aerosol concentrations at Laramie (41°N, 105°W) since 1971 [*Deshler et al*., 2003]. *Kovilakam and Deshler* [2015] present OPC stratospheric aerosol measurements corrected for a previous instrument

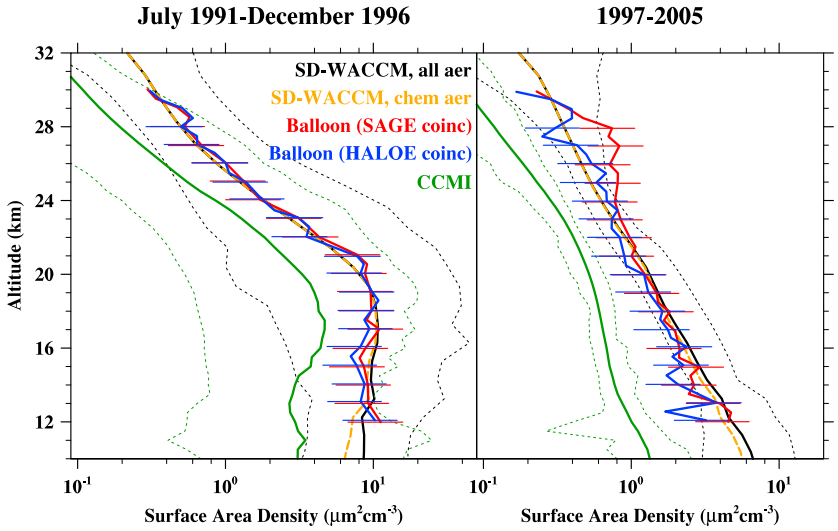

Figure 6. Aerosol surface area density (SAD) profiles calculated in our SD-WACCM VOLC simulation are compared to SAD provided for CCMI experiments [*Arfeuille et al.*, 2014] and to in situ measurements at Laramie (41°N, 105°W) from the University of Wyoming's balloon-borne optical particle counter (OPC) [*Kovilakam and Deshler*, 2015], averaged for (a) July 1991–December 1996 (post-Pinatubo) and (b) 1997–2005 (low volcanic). The solid black curves show mean WACCM SAD for all MAM3 aerosol species, with dashed black curves showing the maximum and minimum monthly-averaged SAD over each time period. Dashed orange curves show WACCM SAD for chemistry, in which sea salt and soil dust have been removed. Mean OPC SAD profiles coincident with SAGE II (red curves) and profiles coincident with HALOE (blue curves) are also shown. The error bars show one standard deviation of the measurements. The solid green curves show the mean CCMI SAD, with dashed green curves showing the maximum and minimum monthly-averaged SAD over each time period.

calibration error. They compare the corrected OPC SAD profiles to satellite extinction measurements from SAGE II and Halogen Occultation Experiment (HALOE). To do so, they averaged OPC profiles that were coincident with measurements from each of the two satellites.

We reproduce the OPC SAD profiles from *Kovilakam and Deshler* [2015] in Figure 6, showing their mean of profiles coincident with SAGE II and with HALOE averaged over two time periods: July 1991–December 1996 (post-Pinatubo) and 1997–2005 (low volcanic). Our WACCM calculated mean SAD profiles for all MAM3 aerosol

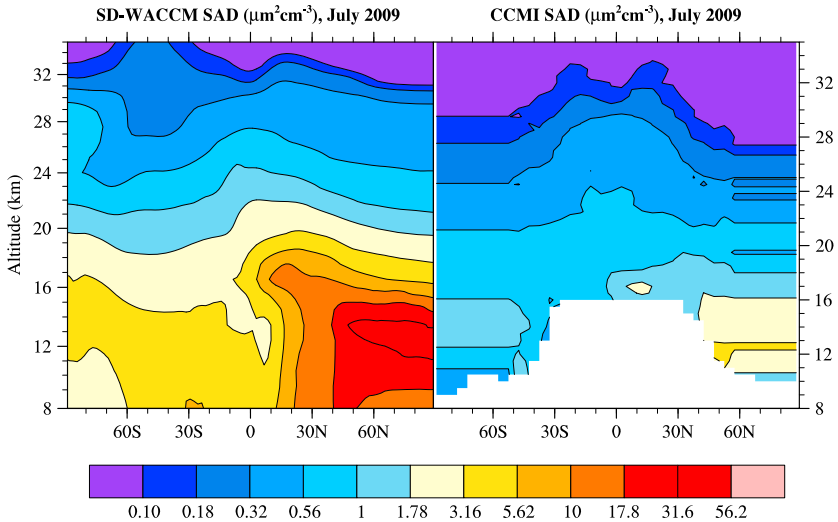

Figure 7. Zonal mean distributions of aerosol surface area density (SAD) for July 2009 (following the June 2009 eruption of Sarychev Peak, 48.1°N, 153.2°E) are compared for (a) SD-WACCM VOLC and (b) the CCMI stratospheric aerosol climatology [*Arfeuille et al.*, 2014].

species show excellent agreement with the OPC measurements during both time periods. The black curves include sea salt and soil dust, which we remove from SAD for the model's heterogeneous chemistry, but which are included in OPC measurements. Our calculated SAD for chemistry, in which sea salt and soil dust have been removed (dashed orange curves), shows the small contribution of those species in the lowermost stratosphere. In contrast, the SAD provided as input to global models for the CCMI experiments [*Arfeuille et al.*, 2013, 2014] is clearly dramatically lower than the OPC SAD. Mean CCMI SAD constitutes roughly 40% of the mean OPC SAD in each period. All of the mean CCMI SAD values are outside of the OPC error bars. The range shown by the green dotted curves makes clear that nearly all of the CCMI monthly SAD values in 1997–2005 are outside of the OPC error bars. *Kovilakam and Deshler* [2015] present a detailed comparison of SAGE version 6 and the revised version 7, which suggests that the algorithm revisions address problems during volcanic periods in particular.

Differences between WACCM SAD and CCMI SAD are even larger immediately following recent moderate volcanic eruptions, such as the June 2009 eruption of Sarychev Peak (48.1°N, 153.2°E), which put 1.2 Tg of SO_2 between 11 and 15 km. Figure 7 shows zonal mean distributions of SAD for July 2009 from WACCM and from CCMI. Our calculated SAD values are generally an order of magnitude larger than those from CCMI. The differences in SAD shown will have significant effects on global stratospheric chemistry. An increase in SAD from 1 to 4 $\mu m^2\,cm^{-3}$ at midlatitudes near 20 km could increase ozone loss rates by 20% or more [*Solomon et al.*, 1996]. Loss rates at high latitudes are even more sensitive to changes in SAD [*Portmann et al.*, 1996].

5. Summary

We have developed a new prognostic capability for calculating global stratospheric aerosol properties based on emissions in CESM. We have compiled a new database of climatically relevant global volcanic SO_2 emissions from 1990–2014 for use in models with prognostic stratospheric aerosol schemes such as CESM, but without ash or ice plume processing. We have developed a new reconstruction of global aerosol properties from 1990 to 2014 based on volcanic and nonvolcanic emissions of sulfur species. Our calculations using CESM1 (WACCM) show remarkable agreement with observations from ground-based lidars and from balloon-borne in situ size-resolved profiles of aerosol concentrations. Our 1990–2014 reconstruction represents a marked improvement over previous stratospheric aerosol forcing data that ignore aerosol extinction below 15 km (a region that can contain the bulk of stratospheric aerosol extinction at midlatitudes and high latitudes) and that are currently being used to force models. In particular, the stark differences in SAOD and SAD compared to other data sets will have significant effects on calculations of the radiative forcing of climate and global stratospheric chemistry over the period 2005–2014. In light of these results, the impact of volcanic aerosols in reducing the rate of global average temperature increases since the year 2000 should be revisited. We have made our calculated aerosol properties from January 1990 to November 2014 available for public download from the Earth System Grid. The data set includes monthly-averaged three-dimensional fields gridded on the model's 96 latitudes, 144 longitudes, and 88 vertical levels. Properties provided include extinction, SAOD, and total AOD at 350, 550, and 1020 nm; SAD for heterogeneous chemistry; SO_4 mass; and aerosol effective radius.

Appendix A: Description of Model Radiation and Chemistry Schemes

In the lower atmosphere, at pressures greater than 0.50 hPa, WACCM calculates heating rates using the CAM5 radiation scheme, the Rapid Radiative Transfer Method for General Circulation Models (RRTMG) [*Mlawer et al.*, 1997; *Iacono et al.*, 2008]. For the upper atmosphere, at pressures less than 0.05 hPa, WACCM computes heating

Table A1. Aqueous and Heterogeneous Reactions in the Troposphere are Consistent With *Lamarque et al.* [2012]

	Bulk Cloud Water	Notes
1	$SO_2 + H_2O_2 \rightarrow S(VI)$	*Tie et al.* [2001] and *Liu et al.* [2012]
2	$SO_2 + O_3 \rightarrow S(VI)$	*Tie et al.* [2001] and *Liu et al.* [2012]
	Tropospheric Aerosols (OC, SO_4, NH_4NO_3, and SOA)	γ = Reaction Probability
3	$N_2O_5 \rightarrow 2 \times HNO_3$	$\gamma = 0.1$
4	$NO_3 \rightarrow HNO_3$	$\gamma = 0.001$
5	$NO_2 \rightarrow 0.5 \times OH + 0.5 \times NO + 0.5 \times HNO_3$	$\gamma = 0.0001$
6	$HO_2 \rightarrow 0.5 \times H_2O_2$	$\gamma = 0.2$

Table A2. Reaction Probabilities (γ) for Stratospheric Heterogeneous Reactions on Liquid Aerosols, Nitric Acid Trihydrate (NAT), and Water Ice are Consistent With *Solomon et al.* [2015]

Reactions	Liquid Aerosols	NAT	H_2O-Ice
$N_2O_5 + H_2O \rightarrow 2 \times HNO_3$	$\gamma \sim 0.1$	$\gamma = 0.0004$	$\gamma = 0.02$
$ClONO_2 + H_2O \rightarrow HOCl + HNO_3$	*Shi et al.* [2001]	$\gamma = 0.004$	$\gamma = 0.3$
$BRONO_2 + H_2O \rightarrow HOBr + HNO_3$	*Shi et al.* [2001]	$\gamma = 0.2$	$\gamma = 0.3$
$ClONO_2 + HCl \rightarrow Cl_2 + HNO_3$	*Shi et al.* [2001]	$\gamma = 0.1$	$\gamma = 0.3$
$HOCl + HCl \rightarrow CL_2 + H_2O$	*Hanson et al.* [1996]	$\gamma = 0.006$	$\gamma = 0.2$
$HOBr + HCl \rightarrow BRCl + H_2O$	*Hanson* [2003]	-	$\gamma = 0.3$

rates using a mesosphere/lower thermosphere (MLT) calculation valid for pressures where the assumption of local thermodynamic equilibrium does not apply [*Marsh et al.*, 2007]. The two codes provide similar results between 0.50 hPa and 0.05 hPa, and we merge the results there with a weighted average of the two methods, using a weighting factor defined by a cubic polynomial in the pressure:

$$w(P) = 0.5 + \frac{3(P - P_{\text{mid}})}{2\Delta P} - 2\left(\frac{P - P_{\text{mid}}}{\Delta P}\right)^3$$

$$\text{where } P_{\text{mid}} = \frac{P_{\text{max}} + P_{\text{min}}}{2}, P_{\text{max}} = 0.50 \text{ hPa}, P_{\text{min}} = 0.05 \text{ hPa}$$

$$\text{and } \Delta P = P_{\text{max}} - P_{\text{min}}.$$

The (merged) heating rate is then computed as

$$Q_{\text{merge}} = w(P)Q_{\text{rrtmg}} + (1 - w(P))Q_{\text{MLT}}.$$

Heating rates applied to the atmosphere are defined purely by RRTMG below the merge region and purely by MLT above the merge region.

Model chemistry includes aqueous-phase and heterogeneous chemistry in the troposphere and stratosphere. SO_2 oxidation in bulk cloud water by H_2O_2 and O_3 (reactions 1 and 2 in Table A1) is based on the Model for Ozone and Related Chemical Tracers treatment of *Tie et al.* [2001]. Further details are provided in the supplement of *Liu et al.* [2012]. Heterogeneous chemistry on tropospheric aerosols (reactions 3–6 in Table A1) are consistent with *Lamarque et al.* [2012]. Heterogeneous reaction rates on stratospheric aerosols and polar stratospheric clouds (PSCs) are consistent with *Solomon et al.* [2015], as shown in Table A2. Surface area densities (SADs) for aerosol reaction are derived from MAM sulfate, carbon, and organic species; sea salt and dust are excluded. SAD for PSCs, composed of supercooled ternary solutions, nitric acid trihydrate (NAT), and water ice, is derived based on MAM sulfate, using the swelling and growth approach described in *Solomon et al.* [2015].

Appendix B: Modal Aerosol Changes for Stratospheric Aerosol

Several changes were made in order to better represent the aerosol size distribution and composition in the stratosphere, particularly under conditions following very high SO_2 emissions. The geometric standard deviation (σ_g) of the accumulation mode was reduced from 1.8 to 1.6. A similar value (1.59) is used in other

Table A3. Modal Aerosol Species for MAM3 are Treated Consistently With *Lamarque et al.* [2012] in the Troposphere[a]

Species	Molecular Mass Formula	Aitken Mode	Accumulation Mode	Coarse Mode
Sulfate (SO_4)	NH_4HSO_4	E	E	X
Primary organic material (POM)	C	-	E	-
Secondary organic aerosol (SOA)	C	X	X	-
Black carbon (bc)	C	-	E	-
Soil dust (dst)	$AlSiO_5$	-	E	E
Sea salt (ncl)	NaCl	E	E	E
Number (num)	-	E	E	E

[a]A molecular mass (column 2) is assigned to each species for advection. MAM3 species in each of the three modes are listed as emitted (E), present but not emitted (X), or not present (−). All MAM3 species are solved using the implicit chemistry solver and are advected and subject to wet and dry deposition. No MAM3 species are subject to prescribed lower boundary conditions.

aerosol microphysical schemes used in the ECHAM5-HAM [*Stier et al*., 2005] and the GLOMAP-mode [*Mann et al*., 2010] models. The coarse mode σ_g was reduced from 2.0 to 1.2. MAM prescribes lower ($D_{gn,lo}$) and upper ($D_{gn,hi}$) limits for the number mode (or median) dry diameter (D_{gn}) of each mode. When the local D_{gn} falls outside these limits, the number concentration of the mode is nudged toward a value that will bring the D_{gn} back within the limits. The accumulation mode $D_{gn,hi}$ was increased slightly from 0.44 μm to 0.48 μm. The coarse mode $D_{gn,lo}$ was reduced from 1.0 μm to 0.4 μm, and the $D_{gn,hi}$ was increased from 4.0 μm to 40.0 μm. Most of the above changes had limited effect on tropospheric aerosols, except for the coarse mode σ_g change, which reduced coarse mode removal rates, requiring some changes to sea salt and dust emissions. Note that σ_g and $D_{gn,lo/hi}$ are constant throughout the entire atmosphere.

Additional changes are applied only in the stratosphere (i.e., above the model-diagnosed local WMO lapse rate tropopause height). MAM3 assumes that sulfate aerosol in the troposphere is ammonium bisulfate and that it is nonvolatile. The MAM gas-aerosol exchange (i.e., condensation/evaporation) module was modified to treat sulfate as aqueous $SO_4^=$ in the stratosphere. The H_2SO_4 equilibrium vapor pressure is calculated as a function of temperature and relative humidity using the empirical relation of *Ayers et al*. [1980] with the correction factor of *Kulmala and Laaksonen* [1990]. Both condensation and evaporation of H_2SO_4 vapor are treated.

Stratospheric concentrations of water vapor are large compared to those for H_2SO_4. *Steele and Hamill* [1981] calculate that water molecules impinge on particles at a rate 10^8 times faster than do H_2SO_4 molecules and that the characteristic timescale for water to equilibrate between the vapor and aerosol phases is of the order of seconds. Model calculations therefore assume that over the model time step for microphysics (30 min), H_2O establishes an equilibrium in which the number of water molecules condensing onto aerosol equals the number evaporating. We use the empirical relation of *Tabazadeh et al*. [1997] to calculate the equilibrium composition (weight fraction H_2SO_4) based on ambient temperature and H_2O specific humidity. Kelvin curvature factors for equilibrium vapor pressures of both H_2SO_4 and H_2O are included in our calculations.

In the standard MAM3 treatment, when Aitken mode particles grow by condensation, some of them are transferred to the accumulation mode. Transfer from accumulation to coarse mode is not treated, as this is a relatively minor process in the troposphere, and the coarse mode does not contain carbonaceous aerosol species. This was modified to treat accumulation to coarse mode transfer and also coarse to accumulation mode transfer above the tropopause. The latter occurs when particles shrink during evaporation and also when coarse aerosols sediment. The coarse mode mass has a higher sedimentation velocity than does coarse mode number, so sedimentation reduces D_{gn} at some altitudes. For transfer associated with particle growth (e.g., accumulation to coarse mode transfer), the algorithm calculates the number and volume of particles in the smaller mode that are greater than a specified cutoff diameter ($D_{gn,cut}$, equal to 0.44 μm for accumulation to coarse) then transfers some or all of this to the larger mode. For accumulation to coarse mode transfer in the stratosphere, the algorithm was further modified so that no transfer occurs when the accumulation mode $D_{gn} < 0.166$ μm and complete transfer occurs when $D_{gn} > 0.47$ μm. Carbonaceous aerosol species are not transferred. For coarse to accumulation mode transfer in the stratosphere, the algorithm was modified to work in the reverse direction (shrinkage rather than growth). No transfer occurs when $D_{gn} > 0.44$ μm and complete transfer occurs when $D_{gn} < 0.41$ μm.

To account for the size distribution changes on the optical properties of the aerosol modes, the coefficients in the aerosol optics parameterization [*Ghan and Zaveri*, 2007] were recalculated. The optical properties in CAM5 are expressed as Chebyshev polynomial functions of a normalized logarithm of the wet (hydrated) surface mode radius, where the coefficients of the polynomials are interpolated bilinearly in complex refractive index, based on Mie calculations of specific scattering, specific absorption, and asymmetry parameter for lognormal size distributions with constant σ_g. Since σ_g has been changed for the accumulation and coarse modes, the coefficients for all refractive indices and wavelengths were recalculated using the *Ghan and Zaveri* [2007] offline code.

Appendix C: Model Initialization

We began our simulations using WACCM in free-running mode with perpetual preindustrial conditions, coupled to a full ocean. The initial ocean state is derived from a coupled preindustrial CAM5 simulation that had reached radiative equilibrium. We used this state to determine the parameterized minimum relative humidity (rhminl = 0.89) for stable low clouds needed in the model for radiative equilibrium in WACCM with preindustrial ocean and atmosphere states. We then used this value for in our subsequent simulations.

For our NOVOLC and VOLC simulations with SD-WACCM, we initialized the atmosphere with a chemical/dynamical condition for 1 January 1990 from an SD-WACCM simulation run for the CCMI, which used a version of the TSMLT mechanism appropriate for WACCM with CAM4 physics. We added to this initial condition spun-up fields for sulfur-bearing gases and MAM3 aerosols for 1 January 1990 derived using WACCM with our modifications to MAM3.

Acknowledgments

We thank David Ridley for providing lidar extinction measurements shown in Figure 5 and Nicolas Theys for providing SO_2 flux data for the database. Mauna Loa lidar data were provided by NOAA ESRL Global Monitoring Division, Boulder, Colorado, USA (http://esrl.noaa.gov/gmd/). Ny-Ålesund lidar data were provided by Christoph Ritter. We thank Anne Smith, Jean-François Lamarque, and two anonymous reviewers for their many helpful comments on this manuscript. The National Center for Atmospheric Research is sponsored by the National Science Foundation. Any opinions, findings, and conclusions or recommendations expressed in the publication are those of the author(s) and do not necessarily reflect the views of the National Science Foundation. S.S. was supported by NSF atmospheric chemistry program grant 1539972. Our global volcanic aerosol reconstruction may be accessed via doi:10.5065/D6S180JM. Supporting data are included as four tables in .xlsx format files and one figure; any additional data, including the source code used for these simulations, may be obtained from M.J.M. (email: mmills@ucar.edu).

References

Andres, R. J., and A. D. Kasgnoc (1998), A time-averaged inventory of subaerial volcanic sulfur emissions, *J. Geophys. Res.*, *103*(D19), 25,251–25,261, doi:10.1029/98JD02091.

Ansmann, A., I. Mattis, U. Wandinger, F. Wagner, J. Reichardt, and T. Deshler (1997), Evolution of the Pinatubo aerosol: Raman lidar observations of particle optical depth, effective radius, mass, and surface area over Central Europe at 53.4°N, *J. Atmos. Sci.*, *54*(2), 2630–2641, doi:10.1175/1520-0469(1997)054<2630:EOTPAR>2.0.CO;2.

Arfeuille, F., B. P. Luo, P. Heckendorn, D. K. Weisenstein, J. X. Sheng, E. Rozanov, M. Schraner, S. Brönnimann, L. W. Thomason, and T. Peter (2013), Modeling the stratospheric warming following the Mt. Pinatubo eruption: Uncertainties in aerosol extinctions, *Atmos. Chem. Phys.*, *13*(22), 11,221–11,234, doi:10.5194/acp-13-11221-2013.

Arfeuille, F., D. K. Weisenstein, H. Mack, E. Rozanov, T. Peter, and S. Brönnimann (2014), Volcanic forcing for climate modeling: A new microphysics-based data set covering years 1600–present, *Clim. Past*, *10*(1), 359–375, doi:10.5194/cp-10-359-2014.

Ayers, G. P., R. W. Gillett, and J. L. Gras (1980), On the vapor pressure of sulfuric acid, *Geophys. Res. Lett.*, *7*, 433–436, doi:10.1029/GL007i006p00433.

Baran, A. J., and J. S. Foot (1994), New application of the operational sounder HIRS in determining a climatology of sulphuric acid aerosol from the Pinatubo eruption, *J. Geophys. Res.*, *99*(D12), 25,673–25,679, doi:10.1029/94JD02044.

Bazhenov, O. E., V. D. Burlakov, S. I. Dolgii, and A. V. Nevzorov (2012), Lidar Observations of aerosol disturbances of the stratosphere over Tomsk (56.5°N; 85.0°E) in volcanic activity period 2006–2011, *Int. J. Opt.*, doi:10.1155/2012/786295.

Bluth, G. J. S., S. D. Doiron, C. C. Schnetzler, A. J. Krueger, and L. S. Walter (1992), Global tracking of the SO2 clouds from the June, 1991 Mount Pinatubo eruptions, *Geophys. Res. Lett.*, *19*(2), 151–154, doi:10.1029/91GL02792.

Bourassa, A. E., A. Robock, W. J. Randel, T. Deshler, L. A. Rieger, N. D. Lloyd, E. J. T. Llewellyn, and D. A. Degenstein (2012), Large volcanic aerosol load in the stratosphere linked to Asian monsoon transport, *Science*, *337*(6090), 78–81, doi:10.1126/science.1219371.

Brühl, C., J. Lelieveld, P. J. Crutzen, and H. Tost (2012), The role of carbonyl sulphide as a source of stratospheric sulphate aerosol and its impact on climate, *Atmos. Chem. Phys.*, *12*(3), 1239–1253, doi:10.5194/acp-12-1239-2012.

Brühl, C., J. Lelieveld, H. Tost, M. Höpfner, and N. Glatthor (2015), Stratospheric sulfur and its implications for radiative forcing simulated by the chemistry climate model EMAC, *J. Geophys. Res. Atmos.*, *120*, 2103–2118, doi:10.1002/2014JD022430.

Chin, M., and D. D. Davis (1995), A reanalysis of carbonyl sulfide as a source of stratospheric background sulfur aerosol, *J. Geophys. Res.*, *100*(D5), 8993–9005, doi:10.1029/95JD00275.

Deshler, T. (2008), A review of global stratospheric aerosol: Measurements, importance, life cycle, and local stratospheric aerosol, *Atmos. Res.*, *90*(2–4), 223–232.

Deshler, T., M. E. Hervig, D. J. Hofmann, J. M. Rosen, and J. B. Liley (2003), Thirty years of in situ stratospheric aerosol size distribution measurements from Laramie, Wyoming (41°N), using balloon-borne instruments, *J. Geophys. Res.*, *108*(D5), 4167, doi:10.1029/2002JD002514.

Dhomse, S. S., et al. (2014), Aerosol microphysics simulations of the Mt. Pinatubo eruption with the UKCA composition-climate model, *Atmos. Chem. Phys. Discuss.*, *14*(2), 2799–2855, doi:10.5194/acpd-14-2799-2014.

Eyring, V., et al. (2013), Overview of IGAC/SPARC Chemistry-Climate Model Initiative (CCMI) community simulations in support of upcoming ozone and climate assessments, *SPARC Newslett.*, *40*, 48–66.

Fahey, D. W., et al. (1993), In situ measurements constraining the role of sulphate aerosols in midlatitude ozone depletion, *Nature*, *363*(6429), 509–514.

Feierabend, K. J., D. K. Havey, S. S. Brown, and V. Vaida (2006), Experimental absolute intensities of the 4ν9 and 5ν9 O–H stretching overtones of H2SO4, *Chem. Phys. Lett.*, *420*(4–6), 438–442, doi:10.1016/j.cplett.2006.01.013.

Fyfe, J. C., K. Salzen, J. N. S. Cole, N. P. Gillett, and J. P. Vernier (2013), Surface response to stratospheric aerosol changes in a coupled atmosphere–ocean model, *Geophys. Res. Lett.*, *40*, 584–588, doi:10.1002/grl.50156.

Gettelman, A., X. Liu, S. J. Ghan, H. Morrison, S. Park, A. J. Conley, S. A. Klein, J. Boyle, D. L. Mitchell, and J. L. F. Li (2010), Global simulations of ice nucleation and ice supersaturation with an improved cloud scheme in the Community Atmosphere Model, *J. Geophys. Res.*, *115*, D18216, doi:10.1029/2009JD013797.

Ghan, S. J., and R. A. Zaveri (2007), Parameterization of optical properties for hydrated internally mixed aerosol, *J. Geophys. Res.*, *112*, D10201, doi:10.1029/2006JD007927.

Guo, S., G. J. S. Bluth, W. I. Rose, I. M. Watson, and A. J. Prata (2004), Re-evaluation of SO2 release of the 15 June 1991 Pinatubo eruption using ultraviolet and infrared satellite sensors, *Geochem. Geophys. Geosyst.*, *5*, Q04001, doi:10.1029/2003GC000654.

Haimberger, L., C. Tavolato, and S. Sperka (2008), Toward elimination of the warm bias in historic radiosonde temperature records—Some new results from a comprehensive intercomparison of upper-air data, *J. Clim.*, *21*, 4587, doi:10.1175/2008JCLI1929.1.

Haimberger, L., C. Tavolato, and S. Sperka (2012), Homogenization of the global radiosonde temperature dataset through combined comparison with reanalysis background series and neighboring stations, *J. Clim.*, *25*(23), 8108–8131, doi:10.1175/JCLI-D-11-00668.1.

Hanson, D. R. (2003), Reactivity of BrONO2 and HOBr on sulfuric acid solutions at low temperatures, *J. Geophys. Res.*, *108*(D8), 4239, doi:10.1029/2002JD002519.

Hanson, D. R., A. R. Ravishankara, and E. R. Lovejoy (1996), Reaction of BrONO2 with H2O on submicron sulfuric acid aerosol and the implications for the lower stratosphere, *J. Geophys. Res.*, *101*(D4), 9063–9069, doi:10.1029/96JD00347.

Haywood, J. M., A. Jones, and G. S. Jones (2013), The impact of volcanic eruptions in the period 2000–2013 on global mean temperature trends evaluated in the HadGEM2-ES climate model, *Atmos. Sci. Lett.*, *15*(2), 92–96, doi:10.1002/asl2.471.

Hintze, P., H. Kjaergaard, V. Vaida, and J. Burkholder (2003), Vibrational and electronic spectroscopy of sulfuric acid vapor, *J. Phys. Chem. A*, *107*(8), 1112–1118, doi:10.1021/jp0263626.

Hoffmann, A. (2011), Comparative aerosol studies based on multi-wavelength Raman LIDAR at Ny-Ålesund, Spitsbergen, Reports on Polar and Marine Research, Bremerhaven, Alfred Wegener Institute for Polar and Marine Research, *630*, 163 p., hdl:10013/epic.37744C.

Hofmann, D. J., and S. Solomon (1989), Ozone destruction through heterogeneous chemistry following the eruption of El Chichon, *J. Geophys. Res.*, *94*, 5029–5041, doi:10.1029/JD094iD04p05029.

Hofmann, D., J. Barnes, M. O'Neill, M. Trudeau, and R. R. Neely III (2009), Increase in background stratospheric aerosol observed with lidar at Mauna Loa Observatory and Boulder, Colorado, *Geophys. Res. Lett.*, *36*, L15808, doi:10.1029/2009GL039008.

Holasek, R. E., S. Self, and A. W. Woods (1996), Satellite observations and interpretation of the 1991 Mount Pinatubo eruption plumes, *J. Geophys. Res.*, *101*(B), 27,635–27,656, doi:10.1029/96JB01179.

Holton, J. R., P. H. Haynes, M. E. McIntyre, A. R. Douglass, R. B. Rood, and L. Pfister (1995), Stratosphere-troposphere exchange, *Rev. Geophys.*, *33*(4), 403–439, doi:10.1029/95RG02097.

Hurrell, J. W. (2008), The climate data guide: Merged Hadley-NOAA/OI sea surface temperature & sea-ice concentration, edited by National Center for Atmospheric Research Staff, *climatedataguide.ucar.edu*. [Available at https://climatedataguide.ucar.edu/climate-data/merged-hadley-noaaoi-sea-surface-temperature-sea-ice-concentration-hurrell-et-al-2008, (Accessed 28 October 2013).]

Hurrell, J. W., et al. (2013), The community Earth system model: A framework for collaborative research, *Bull. Am. Meteorol. Soc.*, doi:10.1175/BAMS-D-12-00121.

Iacono, M. J., J. S. Delamere, E. J. Mlawer, M. W. Shephard, S. A. Clough, and W. D. Collins (2008), Radiative forcing by long-lived greenhouse gases: Calculations with the AER radiative transfer models, *J. Geophys. Res.*, *113*, D13103, doi:10.1029/2008JD009944.

Intergovernmental Panel on Climate Change (2013), *Climate Change 2013: The Physical Science Basis*, edited by T. F. Stocker and D. Qin, Cambridge Univ. Press, Cambridge, U. K.

Jäger, H., and T. Deshler (2002), Lidar backscatter to extinction, mass and area conversions for stratospheric aerosols based on midlatitude balloonborne size distribution measurements, *Geophys. Res. Lett.*, *29*(19), 1929, doi:10.1029/2002GL015609.

Junge, C. E., C. W. Chagnon, and J. E. Manson (1961), Stratospheric aerosols, *J. Meteorol.*, *18*(1), 81–108, doi:10.1175/1520-0469(1961)018<0081:SA>2.0.CO;2.

Kovilakam, M., and T. Deshler (2015), On the accuracy of stratospheric aerosol extinction derived from in situ size distribution measurements and surface area density derived from remote SAGE II and HALOE extinction measurements, *J. Geophys. Res. Atmos.*, *120*, 8426–8447, doi:10.1002/2015JD023303.

Koyaguchi, T., and M. Tokuno (1993), Origin of the giant eruption cloud of Pinatubo, June 15, 1991, *J. Volcanol. Geotherm. Res.*, *55*(1), 85–96, doi:10.1016/0377-0273(93)90091-5.

Kulmala, M., and A. Laaksonen (1990), Binary nucleation of water-sulfuric acid system: Comparison of classical theories with different H2SO4 saturation vapor pressures, *J. Chem. Phys.*, *93*(1), 696–701, doi:10.1063/1.459519.

Kunz, A., L. L. Pan, P. Konopka, D. E. Kinnison, and S. Tilmes (2011), Chemical and dynamical discontinuity at the extratropical tropopause based on START08 and WACCM analyses, *J. Geophys. Res.*, *116*, D24302, doi:10.1029/2011JD016686.

Lamarque, J.-F., et al. (2012), CAM-chem: Description and evaluation of interactive atmospheric chemistry in the Community Earth System Model, *Geosci. Model Dev.*, *5*(2), 369–411, doi:10.5194/gmd-5-369-2012.

Lane, J. R., and H. G. Kjaergaard (2008), Calculated electronic transitions in sulfuric acid and implications for its photodissociation in the atmosphere, *J. Phys. Chem. A*, *112*(22), 4958–4964, doi:10.1021/jp710863r.

Liu, X., et al. (2012), Toward a minimal representation of aerosols in climate models: Description and evaluation in the Community Atmosphere Model CAM5, *Geosci. Model Dev.*, *5*(3), 709–739, doi:10.5194/gmd-5-709-2012.

Mann, G. W., K. S. Carslaw, D. V. Spracklen, D. A. Ridley, P. T. Manktelow, M. P. Chipperfield, S. J. Pickering, and C. E. Johnson (2010), Description and evaluation of GLOMAP-mode: A modal global aerosol microphysics model for the UKCA composition-climate model, *Geosci. Model Dev.*, *3*(2), 519–551, doi:10.5194/gmd-3-519-2010.

Marsh, D. R., R. R. Garcia, D. E. Kinnison, B. A. Boville, F. Sassi, S. C. Solomon, and K. Matthes (2007), Modeling the whole atmosphere response to solar cycle changes in radiative and geomagnetic forcing, *J. Geophys. Res.*, *112*, D23306, doi:10.1029/2006JD008306.

Marsh, D. R., M. J. Mills, D. E. Kinnison, J.-F. Lamarque, N. Calvo, and L. M. Polvani (2013), Climate change from 1850 to 2005 simulated in CESM1(WACCM), *J. Clim.*, *26*, 7372–7390, doi:10.1175/JCLI-D-12-00558.1.

Meehl, G. A., et al. (2012), Climate system response to external forcings and climate change projections in CCSM4, *J. Clim.*, *25*(11), 3661–3683, doi:10.1175/JCLI-D-11-00240.1.

Miller, Y., R. B. Gerber, and V. Vaida (2007), Photodissociation yields for vibrationally excited states of sulfuric acid under atmospheric conditions, *Geophys. Res. Lett.*, *34*, L16820, doi:10.1029/2007GL030529.

Mills, M. J., A. O. Langford, T. J. O'Leary, K. Arpag, H. L. Miller, M. H. Proffitt, R. W. Sanders, and S. Solomon (1993), On the relationship between stratospheric aerosols and nitrogen dioxide, *Geophys. Res. Lett.*, *20*, 1187–1190, doi:10.1029/93GL01124.

Mlawer, E. J., S. J. Taubman, P. D. Brown, M. J. Iacono, and S. A. Clough (1997), Radiative transfer for inhomogeneous atmospheres: RRTM, a validated correlated-k model for the longwave, *J. Geophys. Res.*, *102*(D14), 16,663–16,682, doi:10.1029/97JD00237.

Montzka, S. A., M. Aydin, M. Battle, J. H. Butler, E. S. Saltzman, B. D. Hall, A. D. Clarke, D. Mondeel, and J. W. Elkins (2004), A 350-year atmospheric history for carbonyl sulfide inferred from Antarctic firn air and air trapped in ice, *J. Geophys. Res.*, *109*, D22302, doi:10.1029/2004JD004686.

Morrison, H., and A. Gettelman (2008), A new two-moment bulk stratiform cloud microphysics scheme in the Community Atmosphere Model, Version 3 (CAM3). Part I: Description and numerical tests, *J. Clim.*, *21*, 3642, doi:10.1175/2008JCLI2105.1.

Neale, R. B., et al. (2010), Description of the NCAR Community Atmosphere Model (CAM 5.0), *NCAR Tech. Rep. NCAR/TN-4861STR*.

Neely, R. R., III, J. M. English, O. B. Toon, S. Solomon, M. J. Mills, and J. P. Thayer (2011), Implications of extinction due to meteoritic smoke in the upper stratosphere, *Geophys. Res. Lett.*, *38*, L24808, doi:10.1029/2011GL049865.

Neely, R. R., III, et al. (2013), Recent anthropogenic increases in SO2 from Asia have minimal impact on stratospheric aerosol, *Geophys. Res. Lett.*, *40*, 999–1004, doi:10.1002/grl.50263.

Newhall, C. G., and S. Self (1982), The volcanic explosivity index (VEI) an estimate of explosive magnitude for historical volcanism, *J. Geophys. Res.*, *87*(C2), 1231–1238, doi:10.1029/JC087iC02p01231.

Portmann, R. W., S. Solomon, R. R. Garcia, L. W. Thomason, L. R. Poole, and M. P. McCormick (1996), Role of aerosol variations in anthropogenic ozone depletion in the polar regions, *J. Geophys. Res.*, *101*, 22,991–23,006, doi:10.1029/96JD02608.

Randel, W. J. (2010), Variability and trends in stratospheric temperature and water vapor, in *The Stratosphere: Dynamics, Transport, and Chemistry*, vol. 190, edited by L. M. Polvani, A. H. Soble, and D. W. Waugh, pp. 123–135, AGU, Washington, D. C.

Read, W. G., L. Froidevaux, and J. W. Waters (1993), Microwave limb sounder measurement of stratospheric SO_2 from the Mt. Pinatubo Volcano, *Geophys. Res. Lett.*, *20*(1), 1299–1302, doi:10.1029/93GL00831.

Ridley, D. A., et al. (2014), Total volcanic stratospheric aerosol optical depths and implications for global climate change, *Geophys. Res. Lett.*, *41*, 7763–7769, doi:10.1002/2014GL061541.

Rienecker, M. M., et al. (2011), MERRA: NASA's Modern-Era Retrospective Analysis for Research and Applications, *J. Clim.*, *24*, 3624–3648, doi:10.1175/JCLI-D-11-00015.1.

Rodriguez, J. M., M. K. W. Ko, and N. D. Sze (1991), Role of heterogeneous conversion of N_2O_5 on sulphate aerosols in global ozone losses, *Nature*, *352*(6), 134–137, doi:10.1038/352134a0.

Santer, B. D., et al. (2014), Volcanic contribution to decadal changes in tropospheric temperature, *Nat. Geosci.*, *7*(3), 185–189, doi:10.1038/ngeo2098.
Santer, B. D., et al. (2015), Observed multivariable signals of late 20th and early 21st century volcanic activity, *Geophys. Res. Lett.*, *42*, 500–509, doi:10.1002/2014GL062366.
Sato, M., J. E. Hansen, M. P. McCormick, and J. B. Pollack (1993), Stratospheric aerosol optical depths, 1850–1990, *J. Geophys. Res.*, *98*, 22,987–22,994, doi:10.1029/93JD02553.
Seinfeld, J. H., and S. N. Pandis (1998), Properties of atmospheric aerosol, in *Atmospheric Chemistry and Physics*, pp. 408–451, John Wiley, New York.
Self, S., J.-X. Zhao, R. E. Holasek, R. C. Torres, and A. J. King (1993), The atmospheric impact of the 1991 Mount Pinatubo Eruption.
Sheng, J. X., D. K. Weisenstein, B. P. Luo, E. Rozanov, F. Arfeuille, and T. Peter (2015a), A perturbed parameter model ensemble to investigate 1991 Mt Pinatubo's initial sulfur mass emission, *Atmos. Chem. Phys. Discuss.*, *15*(4), 4601–4625, doi:10.5194/acpd-15-4601-2015.
Sheng, J.-X., D. K. Weisenstein, B.-P. Luo, E. Rozanov, A. Stenke, J. Anet, H. Bingemer, and T. Peter (2015b), Global atmospheric sulfur budget under volcanically quiescent conditions: Aerosol-chemistry-climate model predictions and validation, *J. Geophys. Res. Atmos.*, *120*, 256–276, doi:10.1002/2014JD021985.
Shi, Q., J. T. Jayne, C. E. Kolb, D. R. Worsnop, and P. Davidovits (2001), Kinetic model for reaction of $ClONO_2$ with H_2O and HCl and HOCl with HCl in sulfuric acid solutions, *J. Geophys. Res.*, *106*(D20), 24,259–24,274, doi:10.1029/2000JD000181.
Solomon, S., R. W. Portmann, R. R. Garcia, L. W. Thomason, L. R. Poole, and M. P. McCormick (1996), The role of aerosol variations in anthropogenic ozone depletion at northern midlatitudes, *J. Geophys. Res.*, *101*, 6713–6728, doi:10.1029/95JD03353.
Solomon, S., J. S. Daniel, R. R. Neely III, J. P. Vernier, E. G. Dutton, and L. W. Thomason (2011), The persistently variable "background" stratospheric aerosol layer and global climate change, *Science*, *333*(6044), 866–870, doi:10.1126/science.1206027.
Solomon, S., D. E. Kinnison, J. Bandoro, and R. R. Garcia (2015), Simulation of polar ozone depletion: An update, *J. Geophys. Res. Atmos.*, *120*, 7958–7974, doi:10.1002/2015JD023365.
Stratospheric Processes and their Role in Climate (2010), SPARC CCMVal Report on the Evaluation of Chemistry-Climate Models, edited by V. Eyring, T. G. Shepherd, and D. W. Waugh, *SPARC Rep. 5, WCRP-30/2010, WMO/TD - 40.* [Available at www.sparc-climate.org/publications/sparc-reports/.]
Steele, H. M., and P. Hamill (1981), Effects of temperature and humidity on the growth and optical properties of sulphuric acid—Water droplets in the stratosphere, *J. Aerosol. Sci.*, *12*(6), 517–528.
Stier, P., et al. (2005), The aerosol-climate model ECHAM5-HAM, *Atmos. Chem. Phys.*, *5*(4), 1125–1156, doi:10.5194/acp-5-1125-2005.
Tabazadeh, A., O. B. Toon, S. L. Clegg, and P. Hamill (1997), A new parameterization of H2SO4/H2O aerosol composition: Atmospheric implications, *Geophys. Res. Lett.*, *24*, 1931–1934, doi:10.1029/97GL01879.
Thomason, L. W., and J. P. Vernier (2013), Improved SAGE II cloud/aerosol categorization and observations of the Asian tropopause aerosol layer: 1989–2005, *Atmos. Chem. Phys.*, *13*(9), 4605–4616, doi:10.5194/acp-13-4605-2013.
Thomason, L. W., S. P. Burton, B. P. Luo, and T. Peter (2008), SAGE II measurements of stratospheric aerosol properties at non-volcanic levels, *Atmos. Chem. Phys.*, *8*(4), 983–995, doi:10.5194/acp-8-983-2008.
Tie, X., G. P. Brasseur, L. K. Emmons, L. Horowitz, and D. Kinnison (2001), Effects of aerosols on tropospheric oxidants: A global model study, *J. Geophys. Res.*, *106*(D), 22,931–22,964, doi:10.1029/2001JD900206.
Tilmes, S., et al. (2015), Description and evaluation of tropospheric chemistry and aerosols in the Community Earth System Model (CESM1.2), *Geosci. Model Dev.*, *8*(5), 1395–1426, doi:10.5194/gmd-8-1395-2015.
Uchino, O., et al. (2012), On recent (2008–2012) stratospheric aerosols observed by lidar over Japan, *Atmos. Chem. Phys.*, *12*(24), 11,975–11,984, doi:10.5194/acp-12-11975-2012.
Vaida, V., H. G. Kjaergaard, P. E. Hintze, and D. J. Donaldson (2003), Photolysis of sulfuric acid vapor by visible solar radiation, *Science*, *299*, 1566, doi:10.1126/science.1079297.
Vehkamaki, H., M. Kulmala, I. Napari, K. Lehtinen, C. Timmreck, M. Noppel, and A. Laaksonen (2002), An improved parameterization for sulfuric acid-water nucleation rates for tropospheric and stratospheric conditions, *J. Geophys. Res.*, *107*(D22), 4622, doi:10.1029/2002JD002184.
Vernier, J. P., et al. (2011), Major influence of tropical volcanic eruptions on the stratospheric aerosol layer during the last decade, *Geophys. Res. Lett.*, *38*, L12807, doi:10.1029/2011GL047563.
Wegner, T., D. E. Kinnison, R. R. Garcia, and S. Solomon (2013), Simulation of polar stratospheric clouds in the specified dynamics version of the whole atmosphere community climate model, *J. Geophys. Res. Atmos.*, *118*, 4991–5002, doi:10.1002/jgrd.50415.
Zhao, T. X. P., P. K. Chan, and A. K. Heidinger (2013), A global survey of the effect of cloud contamination on the aerosol optical thickness and its long-term trend derived from operational AVHRR satellite observations, *J. Geophys. Res. Atmos.*, *118*, 2849–2857, doi:10.1002/jgrd.50278.